Life-Cycle Performance and Cost Analysis of Sand Mitigation Measures: Toward a Hybrid Experimental-Computational Approach

Lorenzo Raffaele, Ph.D.[1]; Nicolas Coste, Ph.D.[2]; and Gertjan Glabeke[3]

Abstract: Windblown sand action affects civil structures and infrastructures in sandy environments, such as deserts and coasts. The wind interacts with human built structures of any kind leading to harmful effects, endangering their serviceability and users' safety. To counter it, a number of sand mitigation measures (SMM) have been proposed, primarily through the trial-and-error empirical approach. As such, innovative approaches to properly quantify windblown sand action and to design SMM are needed in the current state-of-art and practice. In this study, the authors propose a novel hybrid approach to derive the life-cycle performance of SMM based on the combination of reliable wind-sand tunnel tests and innovative wind-sand computational simulations. Wind-sand tunnel tests are carried out to characterize the incoming sand flux in open field conditions. In a hybrid approach perspective, wind-sand tunnel measurements allow to properly tuned cheaper wind-sand computational simulations of the full-scale SMM performance. A probabilistic approach for determining windblown sand action and frequencies of sand removal maintenance is applied to a case study on a desert railway. Finally, a life-cycle cost analysis is carried out to assess extra-costs and savings derived from the implementation of the SMM. The proposed approach paves the way toward a comprehensive hybrid approach to the performance assessment of SMM. **DOI: 10.1061/(ASCE)ST.1943-541X.0003344.**

Introduction

Windblown sand hazard affects several civil structures and infrastructures in sandy desert and coastal environments, such as single buildings, farms, towns, solar plants, pipelines, industrial facilities, roads, and railways (Bruno et al. 2018b). On one hand, coastal regions are experiencing the increased frequency of windstorms induced by climate change, giving rise to sand transport events from sandy coasts to built-up areas. On the other hand, desert regions are increasingly hosting human activities and built structures. Within this framework, railway infrastructures are particularly affected given their specific sensitivity to windblown sand and the increasing number of projects currently ongoing and planned in sandy regions across North Africa, Middle East, and Southeast Asia. This allows civil and structural engineering to familiarize with emerging challenging design issues, analogously to other design problems born from other application fields but resulting in key issues in structural engineering (e.g., Ribeiro et al. 2011; Harris et al. 2015).

Windblown sand interacts with surface-mounted human built obstacles of any kind inducing sand erosion and sedimentation around them. From a structural design perspective, windblown sand effects have been categorized into sand limit states (SLS) (Raffaele and Bruno 2019). Sand ultimate limit states (SULS) are defined as the threshold performance level beyond which structures are no longer safe, while attaining sand serviceability limit states implies their loss of functionality. Some examples are shown in Fig. 1: (1) passive lateral sand pressure on a wall and vertical load on a gable roof undermining safety; (2) indoor sand infiltration precluding serviceability; (3) railway full sand coverage compromising train passengers' safety; and (4) permanent rail deformation affecting serviceability, induced by increased stiffness and decreased damping of contaminated ballast bed.

To cope with the effects above, the demand for the development of innovative approaches to properly quantify the so-called windblown sand action (Raffaele and Bruno 2020) and for the design and performance assessment of design solutions to reduce windblown sand induced effects, i.e., sand mitigation measures (SMMs) (Bruno et al. 2018b), has gained momentum in the structural and wind engineering literature.

Windblown sand action has been recently defined as an environmental action in analogy to snow (Raffaele and Bruno 2019). Such an analogy results from their phenomenological and modeling resemblance, but also from the comparable detrimental effects they induce on engineering structures and infrastructures (O'Rourke et al. 2005; Tominaga 2018). On one hand, windblown sand action primarily translates into sand accumulation, giving rise to variable, fixed, static loads directly applied to the affected structure. Remarkably, the Algerian snow and wind code is the sole standard defining global and local distributed vertical sand loads for flat and multispan roofs and providing the sand zone mapping of the country (D.T.R. C 2-4.7 2013). On the other hand, windblown sand translates into

[1]Visiting Professor, Dept. of Environmental and Applied Fluid Dynamics, von Karman Institute for Fluid Dynamics, Waterloosesteenweg 72, B-1640, Sint-Genesius-Rode, Belgium; Assistant Professor, Dept. of Architecture and Design, Politecnico di Torino, Viale Mattioli 39, I-10125 Torino, Italy; Windblown Sand Modeling and Mitigation Joint Research Group, Italy, France (corresponding author). ORCID: https://orcid.org/0000-0002-5549-754X. Email: lorenzo.raffaele@vki.ac.be

[2]Senior Research Engineer, Optiflow Company, Chemin de la Madrague-Ville 160, F-13015 Marseille, France; Windblown Sand Modeling and Mitigation Joint Research Group, Italy, France. Email: coste@optiflow.fr

[3]Senior Test Engineer, Ph.D. Student, Dept. of Environmental and Applied Fluid Dynamics, von Karman Institute for Fluid Dynamics, Waterloosesteenweg 72, B-1640 Sint-Genesius-Rode, Belgium. ORCID: https://orcid.org/0000-0002-4214-0859. Email: glabeke@vki.ac.be

Note. This manuscript was submitted on July 30, 2021; approved on January 25, 2022; published online on May 3, 2022. Discussion period open until October 3, 2022; separate discussions must be submitted for individual papers. This paper is part of the ***Journal of Structural Engineering***, © ASCE, ISSN 0733-9445.

Fig. 1. Windblown sand effects on structures and infrastructures: (a) buried houses in Waldport, Oregon; (b) in In-Salah, Algeria; (c) buried railway track in Namibia; and (d) rail deformation. [Reprinted (a–c) from *Engineering Structures*, Vol. 178, L. Raffaele and L. Bruno, "Windblown sand action on civil structures: Definition and probabilistic modelling," pp. 88–101, © 2019, with permission from Elsevier; reprinted (d) from *Journal of Wind Engineering and Industrial Aerodynamics*, Vol. 177, L. Bruno, M. Horvat, and L. Raffaele, "Windblown sand along railway infrastructures: A review of challenges and mitigation measures," pp. 340–365, © 2018, with permission from Elsevier.]

indirect actions undermining the performance of the built structure/infrastructure and resulting in periodic maintenance operations.

Once more in analogy to windblown snow, several design solutions to mitigate windblown sand effects have been proposed so far (see e.g., Alghamdi and Al-Kahtani 2005; Sañudo-Fontaneda et al. 2011; Basnet et al. 2014). SMMs aim to prevent sand from reaching the protected structure/infrastructure. Most of them are located between the sand source and the protected structure, and they are intended to trap incoming sand by promoting sedimentation [Fig. 2(a)]. As a result, the rigorous design shall be performed by considering both the SMM sand-trapping performance and the environmental loads induced by wind and sand. Such a kind of SMMs usually translates into berms and ditches realized through earthworks [Fig. 2(b)], reinforced concrete porous barriers [Fig. 2(c)], solid barriers [Fig. 2(d)], or a combination of them (Bruno et al. 2018b).

However, with some remarkable exceptions, the rigorous assessment of windblown sand action, and the design and performance assessment of SMMs remain at their early stage in the structural engineering literature, whereas they are mostly based on trial-and-error approaches in the technical practice. According to the authors, this is due to the multidisciplinary and multiphysic nature of the phenomenon coupling fluid dynamics and aeolian processes. As a result, to fill this gap of knowledge, research should benefit from studies in disciplines adjacent and partially overlapping structural engineering (such as wind engineering, applied mathematics, and aeolian geomorphology), and from experimental and numerical approaches.

Physical experiments usually translate into wind tunnel scale tests. wind-sand tunnel (WST) tests have been carried out both on flat ground conditions and around surface-mounted obstacles since the nineteen sixties (White 1996). WST tests allow to reproduce and measure with high accuracy and in a controlled setup the spatial and temporal evolution of wind and sand state variables. Nevertheless, WST tests show some deficiencies related to: (1) the technical difficulty of measuring wind shear stress and sand flux close to the sand bed, and (2) the experimental distortion arising from similarity mismatching related to the impossibility of jointly satisfying all multiphase/multiscale geometric and kinematic similarity requirements when scale models are tested (Raffaele et al. 2021).

Numerical simulations of multiphase flows of relevance to structural engineering applications have dramatically increased in the last several decades, particularly as regards wind-driven rain and windblown snow (see e.g., Kubilay et al. 2013; Tominaga 2018). The numerical simulation of windblown sand flow, herein called erosion-transport-deposition (ETD) simulation, is primarily carried out through the resolution of Eulerian–Lagrangian or fully Eulerian models coupling wind-flow aerodynamics and aeolian processes accounting for the morphodynamic evolution of the sand bed, as reviewed in Lo Giudice et al. (2019). Among them, Eulerian ETD simulations are emerging because they adapt well to the engineering needs of modeling large-scale processes and cutting costs with respect to WST tests. However, they shall be carefully adopted only after their calibration on physical experiments.

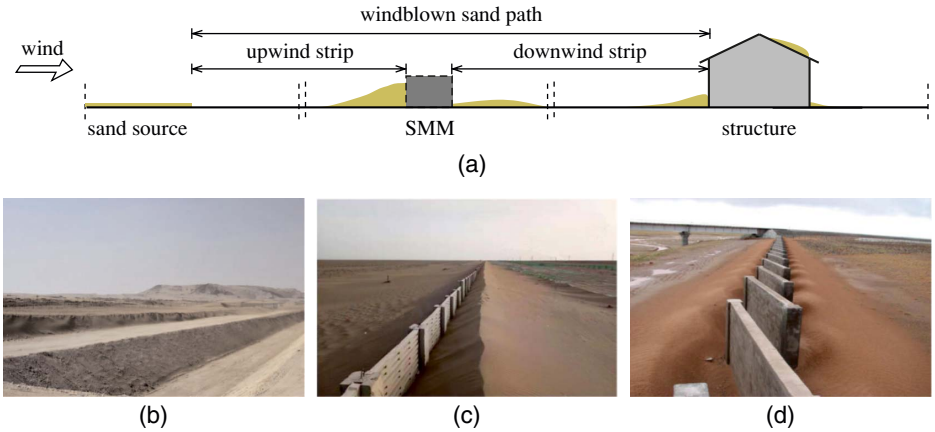

Fig. 2. (a) Conceptual scheme of Sand Mitigation Measure and some examples; (b) berm and ditch; (c) porous barrier; and (d) solid barrier. [Reprinted (b) from Plaza et al. 2012, with permission; reprinted (c) from *Aeolian Research*, Vol. 47, G. Xin, N. Huang, J. Zhang, and H. Dun, "Investigations into the design of sand control fence for Gobi buildings," pp. 100662, © 2021, with permission from Elsevier; reprinted (d) from Guo et al. (2014), under Creative Commons Attribution 4.0 International (CC BY 4.0) license (https://creativecommons.org/licenses/by/4.0/).]

In this study, the authors pave the way towards a novel *hybrid approach* (Meroney 2016) to derive the life-cycle performance (LCP) of SMMs based on the combination of highly reliable WST tests on flat ground conditions, and innovative ETD simulations of the full-scale SMM behavior to overcome the limitations of the standalone methodologies. WST tests are carried out on a flat sand bed to characterize the incoming sand flux in open field conditions. Within a hybrid approach perspective, WST measurements allow to tune cheaper ETD simulations. ETD simulations are carried out by adopting an Eulerian multiphase first order computational fluid dynamics (CFD) model coupling wind flow aerodynamics and sand erosion, transport, sedimentation, and avalanching (Lo Giudice and Preziosi 2020). LCP is assessed through ETD simulations by taking into account the progressive loss of performance of the SMM caused by the gradual accumulation of sand around it. Then, the probabilistic approach to assess windblown sand action and plan sand removal maintenance operations proposed in Raffaele and Bruno (2019) is applied. This allows accounting for multiple uncertainties in environmental in-field conditions, i.e., wind speed, wind direction and threshold velocity for sand erosion, and for their propagation to the resulting windblown sand action. Finally, a life-cycle cost analysis (LCCA) is carried out. The LCCA is increasingly being adopted in the structural engineering domain to evaluate the monetary impact in a performance-based engineering framework (see e.g., Ierimonti et al. 2018; Le and Caracoglia 2019). LCCA allows to assess extra-costs and savings derived from the adoption of the SMM with respect to the unmitigated design scenario. The technical feasibility of the approach is demonstrated by discussing its application to a topical case study dealing with an endangered desert railway.

The paper is organized into four further sections. First, the experimental-computational techniques adopted within the hybrid approach and the modeling framework to assess the life-cycle performance and cost are introduced. The tested case study is introduced, and WST and ETD setups are outlined. Finally, results are discussed and conclusions and perspectives are outlined.

Hybrid Approach

The adopted wind tunnel experimental facility, multiphase computational fluid dynamics model, and probabilistic framework to assess the life-cycle performance and cost analysis are introduced in the following.

Wind Tunnel Facility

The wind tunnel test is carried out in the wind tunnel L-1B of von Karman Institute for Fluid Dynamics. The facility is a closed-circuit wind tunnel with a test section length of about 20 m, and a cross section of height $h_{wt} = 2$ m and width $w_{wt} = 3$ m [Fig. 3(a)].

A low-roughness boundary layer is reproduced to simulate open terrain conditions typical for sand desert. To characterize the clean wind boundary layer, avoiding interference of scattered light from flying sand particles with measuring equipment, a flat wooden board of length $c = 4.9$ m, width $e = 0.3$ m, and thickness 1.8×10^{-2} m with sand grains glued on it was set-up in the rectangular test section [Fig. 3(b)]. A ramp with gentle slope approximately equal to 3° is installed to smooth the transition between wind tunnel floor and the wooden board. The downwind edge is located at the distance $a = 8h_{wt}$ from the inlet of the test section. The reference wind velocity U is measured just upwind of the ramp through Prandtl pitot tube at 0.57 m from the wind tunnel floor. Some initial exploratory tests with a sand bed have been

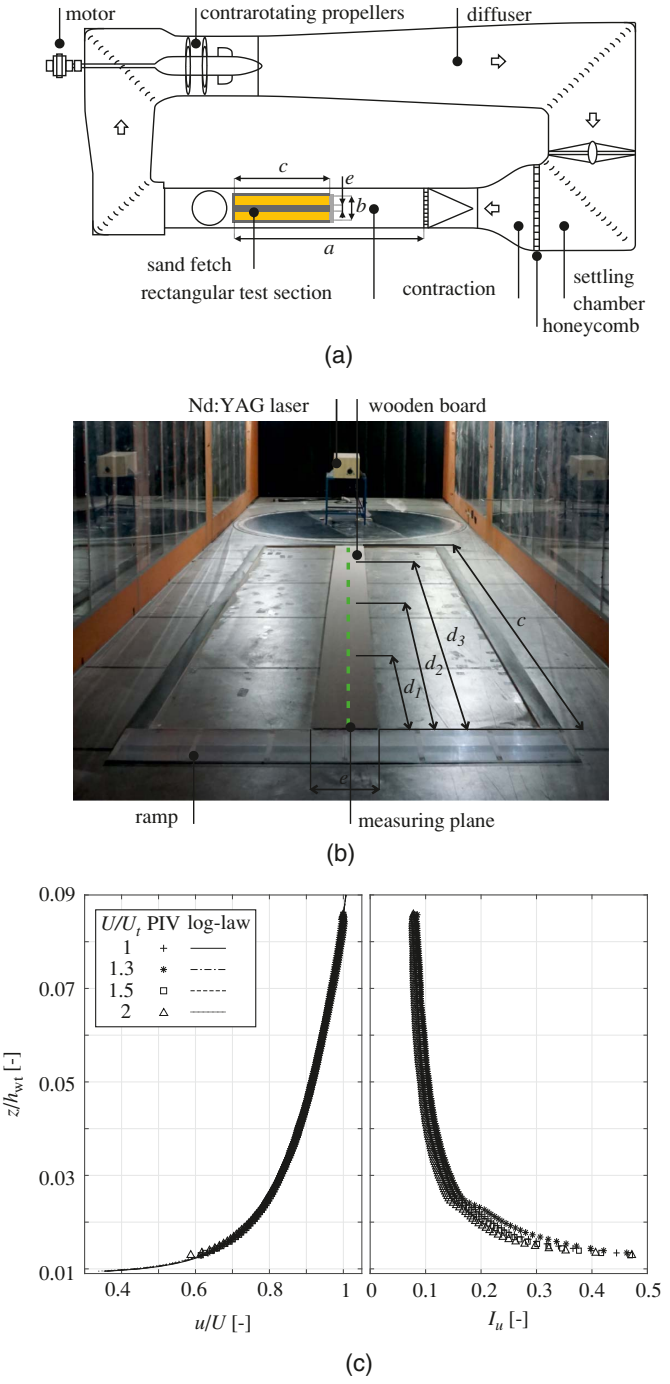

Fig. 3. (a) Plan view of the VKI L-1B wind tunnel; (b) adopted setup to measure wind field; and (c) resulting mean wind speed $u(z)$ and turbulence intensity profiles $I_u(z)$.

performed to ascertain the threshold velocity U_t, defined as the minimum value of the wind speed at which quasisteady sand transport occurs at position d_3. Three increasing wind speeds, respectively, equal to $U = \{1.3U_t, 1.5U_t, 2U_t\}$, are tested.

The mean velocity profile $u(z)$ and mean turbulence intensity profile $I_u(z)$ at the distances $d_2 = 3$ and $d_3 = 4.5$ m from the upwind edge of the wooden board are measured along the test section centerline through particle image velocimetry (PIV) technique adopting a smoke generator to seed the flow with oil particles ranging from 1×10^{-3}–5×10^{-3} mm. Each measurement is taken along the test section centerline to avoid the influence of the

boundary layer developed on the lateral sides of the wind tunnel. A 200 mJ Nd:YAG laser source pulsating at 10 Hz is located far downwind of the measuring section. A laser sheet is generated along the test section centerline and perpendicular to the floor. Its width inevitably varies along the fetch length resulting equal to 8.6, 7.2, and 5.4 mm, respectively, at positions $d_1 = 1.5$, $d_2 = 3$, and $d_3 = 4.5$ m. Two CMOS cameras with resolution $2{,}360 \times 1{,}776$ pixels and a 50 mm objective are located outside the test section to acquire the wind flow field with field of views (FoVs) equal to 18×14 cm. The measured profiles at d_2 and d_3 results are almost unchanged. Fig. 3(c) shows the measured profiles at d_3. The wind speed measurements are fitted with the log-law $u(z) = u_*/\kappa \cdot \ln(z/z_0)$, being u_* the wind shear velocity, $\kappa = 0.41$ the von Karman constant, and z_0 the aerodynamic roughness, leading to $u_* = \{0.25, 0.33, 0.37, 0.51\}$ m/s and $z_0 = 6.5\text{e}-5$ m. The corresponding profile of the streamwise turbulence intensity $I_u(z)$ are included in Fig. 3(c), whereas the related streamwise integral length scales measured at pitot location are $L_u = \{0.17, 0.22, 0.25, 0.36\}$ m.

Computational Model

The wind flow is modeled as an unsteady incompressible turbulent flow through Unsteady Reynolds Average Navier Stokes (URANS) equations. URANS equations are chosen because we are primarily interested in the long-term behavior of the sand transport which induces sand erosion and accumulation around SMMs and which takes place on a much larger time scale than turbulence. The SST $k-\omega$ turbulence model is adopted because of its proven accuracy in simulating wind flow separation around bluff bodies (Menter et al. 2003), such as SMMs. The same CFD model has been validated in Bruno and Fransos (2015) and adopted in Bruno et al. (2018a), Horvat et al. (2020), and Horvat et al. (2021) on the same class of problems, i.e., nominal 2D bluff bodies immersed in a turbulent atmospheric boundary layer. The set of governing equations reads:

$$
\begin{aligned}
&\frac{\partial u_i}{\partial x_i} = 0,\\
&\frac{\partial u_i}{\partial t} + u_j\frac{\partial u_i}{\partial x_j} = -\frac{1}{\rho}\frac{\partial p}{\partial x_i} + \frac{\partial}{\partial x_j}\left[\nu\left(\frac{\partial u_i}{\partial x_j} + \frac{\partial u_j}{\partial x_i}\right)\right] - \frac{\partial}{\partial x_j}(\bar{u}_i' u_j'),\\
&\frac{\partial k}{\partial t} + u_i\frac{\partial k}{\partial x_i} = \frac{\partial}{\partial x_i}\left[(\sigma_k \nu_t + \nu)\frac{\partial k}{\partial x_i}\right] + \tilde{P}_k - \beta^* k\omega,\\
&\frac{\partial \omega}{\partial t} + u_i\frac{\partial \omega}{\partial x_i} = \frac{\partial}{\partial x_i}\left[(\sigma_\omega \nu_t + \nu)\frac{\partial \omega}{\partial x_i}\right] + \alpha\frac{\omega}{k}P_k - \beta\omega^2\\
&\quad + (1-F_1)\frac{2\sigma_\omega}{\omega}\frac{\partial k}{\partial x_i}\frac{\partial \omega}{\partial x_i}
\end{aligned}
\tag{1}
$$

where t = time; ρ = air density; p = average pressure; ν = air kinematic viscosity; ν_t = so-called turbulent kinematic viscosity; k = turbulent kinetic energy; and ω = its specific dissipation rate. The kinetic energy production term $\tilde{P}_k$ is modeled by introducing a production limiter to prevent the build-up of turbulence in stagnation regions, i.e., $\tilde{P}_k = \min(P_k, 10\beta^* k\omega)$, where $P_k \approx 2\nu_t D_{ij}(\partial u_i/\partial x_j)$ and D_{ij} = strain-rate tensor. The standard blending function F_1 and model constants $\beta^* = 0.09$, $\sigma_k = 0.85$, $\sigma_\omega = 0.65$, $\alpha = 0.31$, and $\beta = 0.075$ are obtained from Menter et al. (2003).

Sand-grain roughness wall functions are complemented by SST k-ω turbulence model because of their wide use in computational wind engineering (Blocken et al. 2007) and their proven adequacy from past simulations on the same class of problem (e.g., Liu et al. 2011; Bruno and Fransos 2015). Standard wall functions (Launder and Spalding 1974) with roughness modification (Cebeci and Bradshaw 1977) are applied. The equivalent sand-grain roughness height is determined equal to $k_s = 9.793 z_0/C_s$, where $C_s = 0.5$ is the roughness constant.

The sand phase is considered as a passive scalar and modeled through the conservation equation of sand volume fraction ϕ_s:

$$
\frac{\partial \phi_s}{\partial t} + \frac{\partial q_i}{\partial x_i} = 0 \tag{2}
$$

where the sand flux q_i is given by the combination of advection by wind, sedimentation effects due to gravity, and diffusive flux. In particular:

$$
q_i = u_{s,i}\phi_s + u_{sed}\phi_s + v_{eff}\phi_s\frac{\partial \phi_s}{\partial x_i} \tag{3}
$$

where $u_{s,i}$ = transport velocity of the sand particles by wind taken proportional to u_i, u_{sed} = vertical sedimentation velocity, and ν_{eff} takes into account the mixing-diffusive contribution resulting from the combination of ν_t and the viscous effect due to random collisions at the sand surface $\nu_s = A(2\sqrt{II_{D_{ij}}})^B$, being A and B model parameters to calibrate the concentration profile, and $II_{D_{ij}}$ the second invariant of D_{ij} (Preziosi et al. 2015).

The morphodynamic evolution of the sand surface is accounted for by imposing the continuity of sand flux through the wind-sand interface and the triggering of sand sliding when the sand slope exceeds the critical angle of repose ψ_{cr}, i.e., the steepest slope angle sand grains can pile up. This leads to the modified Exner equation (Lo Giudice and Preziosi 2020):

$$
\frac{\partial h}{\partial t} = v_{av}\frac{\partial}{\partial x_i}\left[\frac{(|\frac{\partial h}{\partial x_i}| - \tan\psi_{cr})_+}{\sqrt{1+|\frac{\partial h}{\partial x_i}|^2}}\frac{\frac{\partial h}{\partial x_i}}{|\frac{\partial h}{\partial x_i}|}\right] + v_{\Sigma,i}^{ED} \tag{4}
$$

where h = height of the wind-sand interface defined on sandy patches only; v_{av} = diffusion coefficient controlling the sliding speed; $(\cdot)_+$ stands for positive part, $v_{\Sigma,i}^{ED} = -[1/(\phi_{cp} - \phi_s)]q_i n_i$ = velocity of the wind-sand interface due to erosion or sedimentation; ϕ_{cp} = sand close-packing volume ratio; and n_i = direction normal to the surface.

Within the framework of this study: (1) steady-state simulations have been carried out on the WST setup to tune the model free parameters, and (2) unsteady simulations have been carried out on the full-scale SMM to assess its LCP. The adopted boundary conditions (b.c.) and 2D computational domains are schematically shown in Fig. 4. Null ϕ_s initial conditions are imposed in the whole domains. No-slip b.c. are imposed at the solid walls. At the inlet, Neumann zero-gradient b.c. is imposed for p and ϕ_s, whereas Dirichlet b.c. is imposed on u, k, ω. At the outlet, Neumann zero-gradient b.c. is imposed for all flow variables, except for Dirichlet b.c. for p. Concerning the WST domain, the inlet profile of u is prescribed using the power law $u(z) = U[2z/h_{wt}]^{1/n}$ for turbulent boundary layer, whereas the inlet profile of k and ω are set constant and equal to $k = 3/2(UI_u)^2$ and $\omega = \sqrt{k}/(0.09^{0.25}L_u)$. Concerning the full-scale SMM domain, a log-law inlet u profile is set, whereas the profiles of k and ω are set in accordance to Richards and Norris (2011) to replicate a neutral atmospheric boundary layer, and symmetry b.c. is imposed at the top. Finally, a Dirichlet sand erosion b.c. is set to properly model erosion on sandy surfaces, whereas a Neumann b.c. is imposed on nonerodible surfaces. In particular, erosion occurs when the wind shear velocity u_* is higher than the threshold one u_{*t} (Kok et al. 2012). According to Ho et al. (2011):

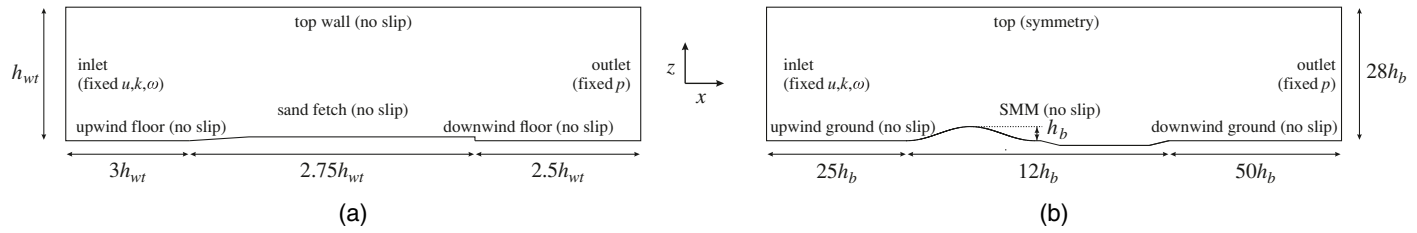

Fig. 4. Scheme of computational domain and boundary conditions: (a) WST domain; and (b) full-scale SMM domain.

$$-v_{eff}\phi_s \frac{\partial \phi_s}{\partial x_i} n_i = A_H \rho \sqrt{\frac{\bar{d}}{g}} (u_*^2 - \hat{u}_{*t}^2)_+ \tag{5}$$

where A_H = model parameter depending on the physical properties of the sand; $\bar{d}$ = mean sand diameter; g = acceleration due to gravity, and $\hat{u}_{*t}$ directly follows from u_{*t} and takes into account the local effect due to inclined slopes; and $\hat{u}_{*t}^2 = u_{*t}^2(\cos\psi + \sin\psi/\tan\psi_{cr})$ being ψ the ground slope angle (Iversen and Rasmussen 1994).

Space discretization follows a predominantly structured grid of hexahedral control volumes. The mesh is refined close to the ground, so that the height n_w of the wall-adjacent cell: (1) provides a sufficiently high mesh resolution along the normal direction to the surface to adequately resolve the gradients of wind-sand state variables, and (2) complies with the wall function requirement on dimensionless wall unit $30 < n^+ = n_p u_* / \nu < 200$, being $n_p = n_w/2$ the cell center height. The total number of cells for WST and full-scale SMM domains is equal to about $3.6 \times 10^{+4}$ and $1.6 \times 10^{+5}$, respectively.

The cell center values of the state variables are interpolated at face locations using the second-order central difference scheme for the diffusive terms. The convection terms are discretized by means of the so-called limited linear scheme. SIMPLE and PIMPLE algorithms are used for pressure-velocity coupling for steady-state and unsteady cases, respectively. The finite volume open source code OpenFOAM© is adopted. On average, a CPU time of about 1.5 h is required for each steady-state simulation and a CPU time from 72 to 96 h is required for each unsteady simulation on Intel(R) Core(TM) dual-processor Sandy Bridge server @ 2.6 GHz with 16 cores employed.

Life-Cycle Performance and Cost Analysis

The modeling framework to assess windblown sand action on a generic surface-mounted obstacle is shown in Fig. 5(a). The sand transport under open field conditions is commonly quantified by the incoming sand transport rate Q_0, defined as the integral over the vertical direction z of the sand flux $q(z)$. In the present study, Q_0 is quantified by taking into account the probabilistic description of u_* and u_{*t} (Raffaele and Bruno 2019) through the semiempirical expression:

$$Q_0 = 6.7 \sqrt{\frac{\bar{d}}{d_r}} \frac{\rho}{g} u_*^3 \left[1 - \frac{u_{*t}|\bar{d}}{u_*}\right]_+ \tag{6}$$

where $d_r = 0.25$ mm is a reference sand grain diameter. Whenever Q_0 encounters an obstacle, it splits into sedimentation rate $Q_{s,1}$ and outgoing transport rate Q_1. In turn, the windblown sand action results from the time-cumulated $Q_{s,1}$ and translates into the accumulated sand volume V_1.

Within this framework, the life-cycle performance of the ith obstacle is expressed by the sand trapping efficiency $e_i = (Q_{i-1} - Q_i)/Q_{i-1}$. e_i which depends on the sand transport direction θ and on the overall obstacle shape, that depends in turn on the initial geometry Γ_0 and on the volume of sand sedimented around it, V. Therefore, the resulting accumulated sand volume V_i after time t is given by the random sum:

$$V_i(t) = \sum_{n=1}^{N_\theta} e_i(\theta, \Gamma_0, V_i) Q_{i-1,n} \Delta t \tag{7}$$

where $Q_{i-1,n}$ = independent and identically distributed copies of Q_{i-1}; Δt = sampling interval of the wind speed; and N_θ = number of sand transport occurrences along the direction θ over time t. The basic condition for a satisfactory state is given by $V_i(t) < V_{R,i}$, being $V_{R,i}$ the resistant sand volume. From this, the probability of failure $p_{f_i}(t)$ results equal to:

$$p_{f_i}(t) = P[V_i(t) > V_{R,i}] = \int_{V_{R,i}}^{+\infty} f_{V_i}(x,t)dx = 1 - F_{V_i}(V_{R,i}, t) \tag{8}$$

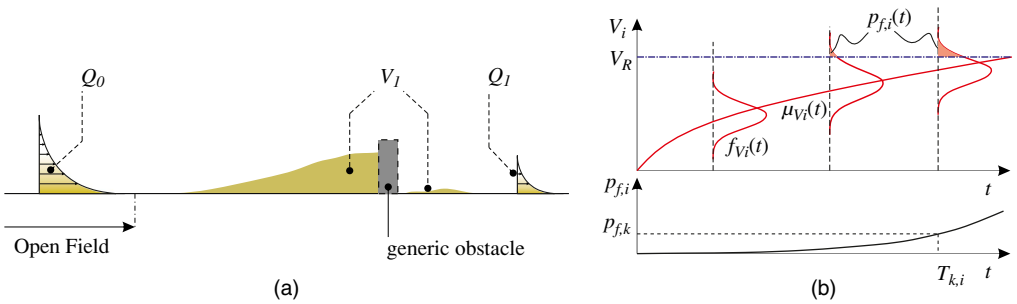

Fig. 5. Windblown sand action: (a) conceptual scheme; and (b) probability of failure.

where f_{V_i} and F_{V_i} = probability density and cumulative distribution functions of V_i, respectively. As a result, the characteristic time of failure $T_{k,i}$ is given by:

$$T_{k,i} = p_{f_i}^{-1}(p_{f,k}) = \inf\{t \geq 0 : F_{V_i(t)}(V_{R,i}) \leq 1 - p_{f,k}\} \quad (9)$$

where $p_{f,k}$ = characteristic probability of failure. Fig. 5(b) sketches the generic trend of the time-variant sand action through its density $f_{V_i}(t)$, the mean value $\mu_{V_i}(t)$, and the increasing trend of the probability of failure $p_{f_i}(t)$.

Finally, LCCA (Fabrycky and Blanchard 1991) can be carried out based on $T_{k,i}$, considering the cost of SMM design and construction c_d, and sand maintenance related costs associated with the ith obstacle $c_{s,i}$:

$$c(t_L) = \sum_{t=1}^{t_L} \left[\frac{c_d/T_d + \sum_{i=1}^{N} c_{s,i}/T_{k,i}}{(1+r)^t} \right]$$
$$\text{with } c_d = 0 \text{ if } t > T_d \text{ and } c_{s,i} = 0 \text{ if } t \leq T_d \quad (10)$$

where $c(t_L)$ = cumulated life-cycle cost at time t_L; T_d = time required for SMM design and construction; N = the number of infrastructure components inducing V_i; and r = the discount rate.

Setup of the Study

Study Layout

The proposed hybrid approach is applied to a case study railway segment located near Al Ain along the Ethiad Rail line in the United Arab Emirates. The chosen site is threatened by the sand of Rub' al-Khali desert. The examined railway segment develops along the NE-SW direction. The local sand granulometry is composed of fine grained, moderately well-sorted sand with mean diameter $\bar{d} = 0.16$ mm (Edgell 2006). The probability density function of u_{*t} is derived from Raffaele et al. (2016) as a function of $\bar{d}$. Conversely, the probability density functions of u_* is derived from an anemometric station in proximity of Al Ain. The employed dataset of the 10 min average wind velocity U_{10} at 10 m from the ground refers to 10 years, from January 2008 to December 2017. The time sampling corresponds to 1 h, whereas the yaw angle discretization is equal to 10°. The aerodynamic roughness length is set equal to $z_0 = 3\text{e}-3$ m, according to the recommendations given in EN 1991-1-4 (CEN 2005).

Fig. 6 shows the windblown sand action modeling framework and the related state variables for a single side of the railway infrastructure. The same scheme is mirrored for the opposite side. Such a scheme directly results from the general one in Fig. 5, by putting in series three successive obstacles, i.e., the SMM ($i = 1$), the embankment ($i = 2$), and track ($i = 3$). The berm and ditch is a well-known SMM for desert railway applications [see e.g., Phillips (2011)]. Here, we investigate a generalization of it. The tested SMM results from the combination of a $h_b = 3$ m high $l_b = 20$ m long berm, followed by a $h_d = 1$ m deep $l_d = 20$ m long ditch. The berm follows the sinusoidal profile $z = h_b/2 \sin[2\pi/l_b(x - l_b/4))] + h_b/2$. The ditch side walls are inclined with 1/3 slope gradient. The height of the embankment is set equal to $h_e = 2.5$ m. A double-track railway is considered, with a $h_r = 0.25$ m deep ballast bed and a 5 m wide line-side access track.

The LCP of the SMM is obtained through the proposed hybrid approach. The LCP of the embankment is derived from WST tests in Hotta and Horikawa (1990), whereas the LCP of the railway track is conjectured maximum and constant up to the filling of ballast voids and then linearly decreasing until it reaches its full capacity V_f, in analogy to Raffaele and Bruno (2020). $V_{R,1}$ and $V_{R,2}$ are set equal to the volume corresponding to 80% and 50% of the initial value of e_i, respectively. Conversely, $V_{R,3}$ is set equal to the volume giving rise to the SULS at full rail coverage.

The LCCA spans the whole service life of the infrastructure, set equal to $t_L = 100$ years. The railway construction time is set equal to $T_d = 6$ years. The costs retained in the LCCA comprehend: (1) SMM design and construction $c_d = \$790/\text{m}$, (2) removal and disposal of accumulated sand around the SMM $c_{s,1} = \$7/\text{m}^3$ and embankment $c_{s,2} = \$7.7/\text{m}^3$, (3) railway ballast cleaning $c_{s,3} = \$56/\text{m}$. For the sake of generality, the discount rate is set equal to $r = 5\%$, whereas costs induced by land expropriation due to SMM construction and by loss of capacity due to sand maintenance operations are not considered in the present study. Indeed, they go beyond the single analyzed railway segment and highly depend on the specific features of the whole railway network and country economic system.

Wind-Sand Tunnel Test Setup

A flat sand bed of length $b = 4.9$ m, width $w = 1.8$ m, and thickness 1.8×10^{-2} m has been set up in the wind tunnel test section replacing the wooden board [Fig. 7(a)]. The sand bed is confined by wooden slats and fillet to the wind tunnel floor through the upwind ramp in analogy with the setup proposed by Tominaga et al. (2018).

The particle size distribution of the tested sand has been obtained through microscopic imaging technique and is plotted in Fig. 7(b) through its cumulative distribution $F(d)$. The mean grain diameter is equal to $\bar{d} = 0.147$ mm, very close to the one on site. The threshold shear velocity obtained through preliminary wind tunnel tests results equals to $u_{*t} = 0.245$ m/s (corresponding to $U_t = 5.54$ m/s). Such a value of u_{*t} agrees with past wind tunnel measurements on sand samples with same $\bar{d}$ (see e.g., Raffaele et al. 2016).

Three tests have been performed by progressively increasing the incoming wind speed $U = \{1.3U_t, 1.5U_t, 2U_t\}$. Each test started

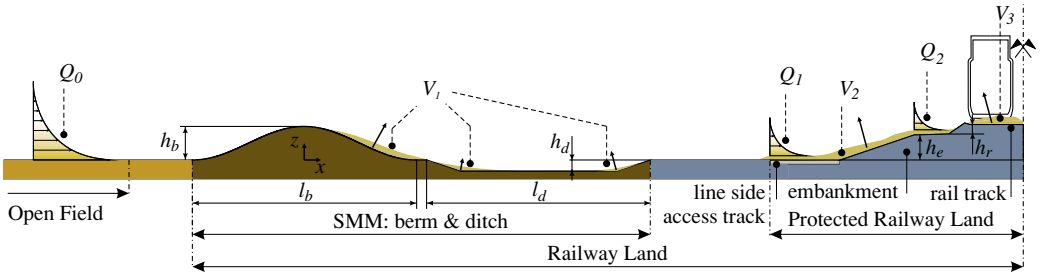

Fig. 6. Modeling framework of windblown sand accumulation around the mitigated railway infrastructures case study.

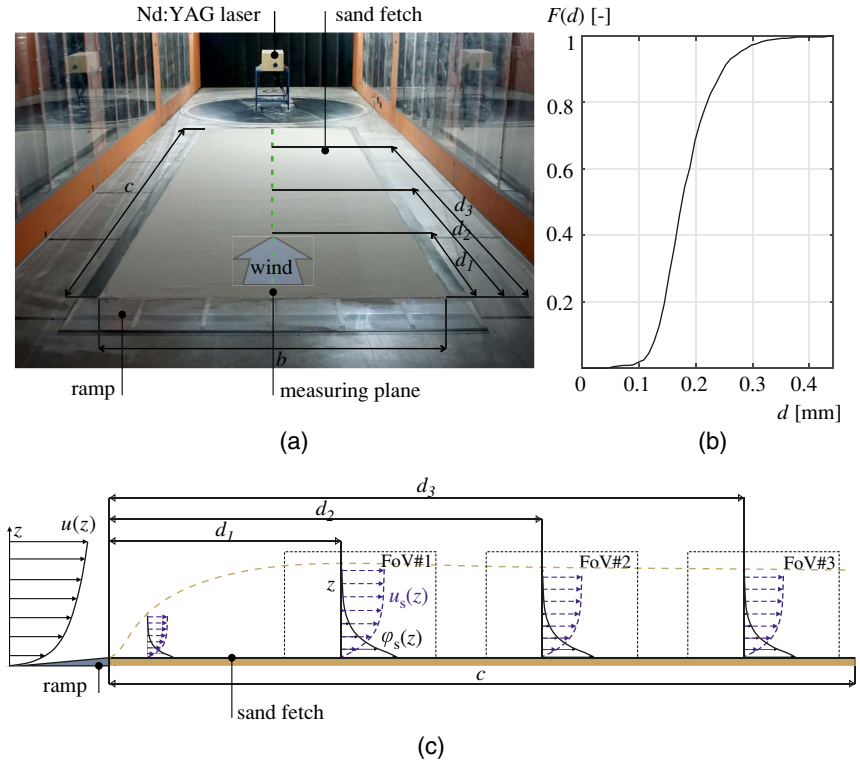

Fig. 7. (a) Wind-sand tunnel test setup; (b) tested sand particle size distribution; and (c) scheme of the measuring cross section with FoVs for PTV measurements.

from the same initial condition, a perfectly flat uniform sand bed, and lasted $T = 300$ s to ensure reaching a quasisteady sand transport. To ensure repeatability, each test has been performed twice. The similarity of the saltation layer with respect to open field condition is taken into account by: (1) assuring that the wind flow is fully rough, i.e., the friction Reynolds number satisfies the criterion $\mathrm{Re}_* \approx u_*^3/2g\nu = [53, 454] > 30$ (Anno 1984), (2) avoiding disturbance in streamwise pressure by satisfying the Froude number criterion, i.e., $\mathrm{Fr} = U^2/h_{wt}g = [1.24, 5.27] < 20$ (White 1996), and (3) adopting a long sand fetch equal to $b = 4.9$ m to ease sand transport saturation and let the wind flow adjust to the sand z_0 (Kok et al. 2012).

The installed measuring equipment allows for the detection of the instantaneous sand particles concentration $\phi(z, t)$ and velocity $u_s(z, t)$ over the flat sand bed through particle tracking velocimetry (PTV). The laser source pulsates at 2 Hz. The two CMOS cameras are moved along the sand fetch to acquire PTV pictures in d_1, d_2, and d_3. The acquired FoVs are sketched in Fig. 7(c). The velocity and concentration fields of sand particles are detected with 55×40 cm^2 FoVs for each position, with a 35 mm objective.

Wind-Sand Computational Simulations: Incoming Wind Flow and Sand Features

The incoming wind flow features differ as a function of the computational domain. On the one hand, the incoming wind flow of the WST scale simulation reflects the experimental conditions. The ground aerodynamic roughness length is set equal to $z_0 = 6.5 \times 10^{-5}$ m, according to the boundary layer PIV measurements. The free parameter of the inlet wind speed power law is set to reproduce the wind speed profiles measured at d_2 and d_3, resulting in $n = 10$. On the other hand, the incoming wind flow of the SMM full-scale simulations reflects actual desert conditions. The ground aerodynamic roughness length is set equal to $z_0 = 3\mathrm{e}-3$ m. The incoming wind shear velocity is set equal to $u_* = 2u_{*t} = 0.49$ m/s to exceed u_{*t} and induce windblown sand transport upwind from the SMM. During sand transport events, the lower bound ($u_* = u_{*t}$) of the reference wind speed at the top of the berm is equal to $u_{h_B} = 4.21$ m/s, and the corresponding Reynolds number is $\mathrm{Re_{hB}} = 8.5 \times 10^5$. In the case of nominally 2D sinusoidal berms, such a value suggests that the flow triggering windblown sand transport is predominantly within the Reynolds supercritical regime (Ferreira et al. 1995). As such, significant Reynolds effects are not expected to take place for $u_* > u_{*t}$.

For both computational domains, the adopted sand diameter is set equal to the mean value of the tested sand, i.e., $\bar{d} = 0.147$ mm. The corresponding mean values of threshold shear velocity and sedimentation velocity are respectively set equal to $u_{*t} = 0.245$ m/s, in accordance to wind tunnel PIV measurements, and to $u_{sed} = 0.782$ m/s, according to the statistical characterization proposed in Raffaele et al. (2020). Finally, the remaining model constants are set equal to $\nu_{av} = 0.1$ m^2/s, $\psi_{cr} = 32°$, and $\phi_{cp} = 0.6$.

The adopted time step in unsteady ETD simulations is set equal to $\Delta t_s = 1\mathrm{e}-3$ s, giving rise to a maximum Courant number $C \approx 0.4$. Given the time demanding unsteady multiphase simulations, the whole problem is decomposed into shorter simulations to assess the discrete piece-wise LCP. For each tested sand level: (1) an unsteady ETD simulation is carried out up to reaching of quasisteady sand transport conditions by assuring the convergence of incoming and outgoing sand transport rates, (2) LCP is assessed, (3) a new geometry corresponding to a new extrapolated sand level is obtained by shifting the wind-sand interface proportionally to the local value of the erosion-deposition velocity v_Σ^{ED}, and (4) a new mesh is built on the obtained geometry. The above steps are

repeated systematically to describe the trend of LCP, up to reaching null SMM performance, i.e., sand flux at inflow equal to sand flux at outflow. The shifting Δh of the wind-sand interface is done manually relying on $v_{\Sigma}^{ED}\Delta t$, being Δt an arbitrarily chosen time interval. As such, the convergence of sand transport shall be assured for each extrapolated sand level.

Results

In the following, the tuned steady ETD simulations are compared with WST measurements, then SMM life-cycle performance is assessed through unsteady ETD simulations. Finally, the time-varying windblown sand action is quantified on the considered case study and life-cycle cost analysis is applied. The proposed hybrid approach can be applied to any kind of structure/infrastructure as long as the LCP of any affected obstacle is available. At the time being, scarce laboratory measurements and even more scarce computational simulations only allow for the quantification of the LCP in the railway infrastructure domain.

Comparison between WST Measurements and ETD Results

Steady-state ETD simulations are tuned on WST measurements by setting the value of free parameters in Eqs. (3) and (5). In this section, the comparison between time-averaged WST measurements and ETD results is provided. In particular, Fig. 8 collects the vertical profiles of the sand volume fraction $\phi_s(z)$, streamwise component of the sand velocity $u_s(z)$, and flux $q(z)$ at positions d_1 (a,d,g), d_2 (b,e,h), and d_3 (c,f,i), providing the mean value μ and standard deviation σ.

The sand volume fraction follows the typical exponentially decreasing law $\mu_{\phi_s(z)} = \gamma e^{-z/\lambda}$ (Ho et al. 2011). For a given position, the rate of decay of $\phi_s(z)$ is almost the same for $u_*/u_{*t} = 1.3$ and $u_*/u_{*t} = 1.5$, whereas it sensibly varies for $u_*/u_{*t} = 2$. Conversely, for a given wind speed, $\phi_s(z = 0)$ increases streamwise. According to the authors, the lower than expected $\mu_{\phi_s(z)}$ and high $\sigma_{\phi_s(z)}$ in d_1 for $u_*/u_{*t} = 1.3$ are caused by the experienced intermittent unsteady sand transport induced by u_* still close to the threshold and the short fetch length. Indeed, the adopted first order ETD model is not able to capture such out-of-equilibrium erosion conditions. Discrepancies in ϕ_s between WST and ETD fade out with the increasing of sand fetch.

The sand velocity profiles can be divided into two layers resulting from strong variation of ϕ_s (Valance et al. 2015). Within the near-wall region where $\phi_s(z)$ is high ($z/h_{wt} < 0.01$), $u_s(z)$ is weakly sensitive to u_* and linearly increasing with z. Conversely, where $\phi_s(z)$ is low ($z/h_{wt} > 0.01$), $u_s(z)$ is highly sensitive to u_* and follows a logarithmic-like increasing trend. Despite the overall promising matching of profiles for a first order model, ETD simulations are not able to reproduce $u_s \neq 0$ at the ground, and particularly overestimates u_s close to the ground ($0 < z/h_{wt} < 0.015$) for $u_*/u_{*t} = 2$. The ETD first order model suits well highly diluted flows (i.e., far from the sand bed), whereas it shows some

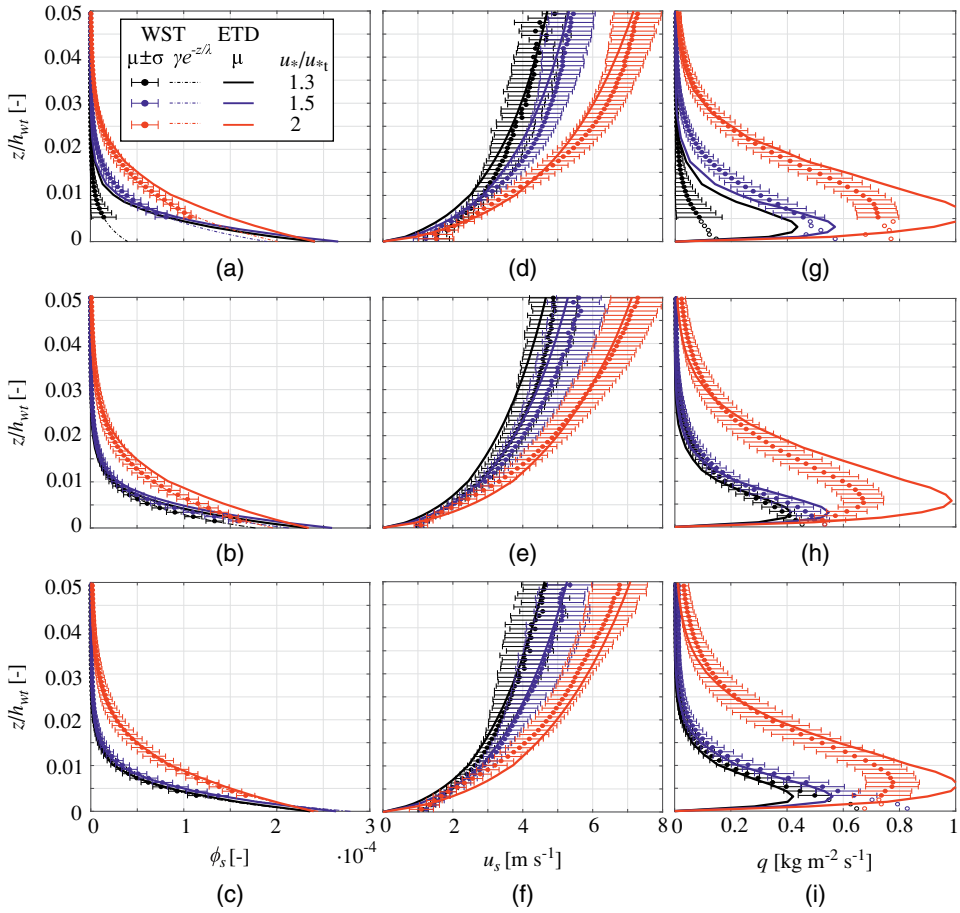

Fig. 8. Vertical profiles of (a–c) sand volume fraction ϕ_s; (d–f) velocity u_s; and (g–i) flux q_s from WST measurements and ETD simulations at positions (a, d, and g) $d1$, (b, e, and h) $d2$, and (c, f, and i) $d3$.

deficiency close to the wall where sand concentration is high (Lo Giudice et al. 2019).

The longitudinal sand flux directly results from $q(z) = \rho_s \phi_s(z) u_s(z)$, being $\rho_s = 2{,}650$ kg/m^3 the sand density. Whenever ϕ_s measurements were missing close to the wall due to nonuniform laser reflections, $\phi_s(z)$ is extrapolated from fitted exponentially decreasing functions [see blank circles in Figs. 8(g–i)]. For $u_*/u_{*t} = \{1.3, 1.5\}$, the measured profiles follow a typical decreasing exponential trend. Conversely, for $u_*/u_{*t} = 2$ the trend is no more monotonic and a maximum appears at about $z/h_{wt} = 0.005$, analogously to e.g., Raffaele et al. (2021). The discrepancies in $\phi(z)$ and $u_s(z)$ between WST and ETD propagate to $q(z)$ giving rise to: (1) the strong mismatching in d_1 for $u_* = 1.3u_{*t}$, (2) the nonnegligible overestimation in correspondence of the maximum value of $q(z)$ for $u_*/u_{*t} = 2$, and (3) the nonphysical null values of $q(z)$ at the wall.

Finally, sand transport rate is evaluated to ascertain discrepancies between WST and ETD in bulk terms. The convergence in time is quantitatively checked by means of the weighted residual Q_{res} of the mean value of sand transport rate Q. The weighted residual is defined for growing dimensionless time $t^* = tU/0.5h_{wt}$ as $Q_{res} = |Q(t^*) - Q(t^* - \Delta t^*)|/Q(t^*)$. The obtained results are plotted in Fig. 9(a) for $u_*/u_{*t} = 2$, for the sake of conciseness. For each position, the trend of convergence $Q_{res} \sim 1/t^*$ gives rise to $Q_{res} = 1\mathrm{e}-3$ at about $t^* = 1\mathrm{e}-3$, consistently with Raffaele et al. (2021). Pointwise Q measurements and ETD results are compared in Fig. 9(b). For $u_*/u_{*t} = \{1.3, 1.5\}$, ETD results overall quantitatively agree well with WST measurements (apart from $x = 1.5$ m $u_*/u_{*t} = 1.3$). For $u_*/u_{*t} = 2$, the mismatching between WST and ETD is significant. In particular, ETD overestimates WST results. WST discrepancies may be related to the longer fetch required to reach equilibrium conditions due to the higher u_*, as highlighted in Dong et al. (2004).

SMM Life-Cycle Performance

The wind flow features around the SMM are characterized though a steady RANS CFD simulation. Fig. 10(a) shows the wind flow topology around the clean SMM by means of streamlines coupled with a vorticity magnitude field. The vorticity magnitude is high close to the wall due to the atmospheric boundary layer, whereas the outer free flow is quasiirrotational. The boundary layer separates on the berm downwind slope, inducing a large clockwise vortex. The recirculation area is characterized by the coalescence of two smaller vortices, respectively, induced by the berm and by the ditch. The wind flow then reattaches within the ditch and accelerates along its downwind slope. The vertical dimensionless wind speed profiles u/u_{h_b} upwind (p1), across (p2, p3, p4), and downwind (p5) from the SMM are plotted in Fig. 10(b) versus the dimensionless height $(z - z_g)/h_b$, being z_g the ground height, to further examine the wind flow pattern. p1 shows the upwards flow deflection induced by the berm, that results in a decrease of u and $\partial u/\partial z|_{z=0}$. p2 shows a significant flow acceleration induced by the berm upwind slope resulting in an increment of u close to the ground and $\partial u/\partial z|_{z=0}$. p3 and p4 are located within the recirculation region. p3 is located just downwind the berm, showing a large negative $\partial u/\partial z|_{z=0}$. p4 is located within the ditch and closer to the reattachment point, showing an overall lower wind speed magnitude and $\partial u/\partial z|_{z=0}$ compared with p3. p5 is located downwind the ditch showing progressive wind speed recovery and a weak $\partial u/\partial z|_{z=0}$.

To assess the full-scale SMM life-cycle performance e_1, unsteady ETD simulations are carried out starting from the above-mentioned wind flow initial condition. Nine consecutive ETD simulations have been carried out to describe the morphodynamic evolution of the sand bed, starting from the clean SMM (fill 0) up to its complete filling (fill 8). Fig. 10(c) shows the multiphase flow topology around the SMM by means of wind flow streamlines coupled with a dimensionless sand concentration field, for the increasing filling levels 0, 4, 6, and 7. Sand is eroded from the upwind side of the SMM and gradually transported downwind. Sand starts depositing along the berm upwind foot and upwind slope due to the upwards flow deflection highlighted in p1 [Fig. 10(b)]. After that, sand climbs over the berm due to wind flow acceleration and progressively deposits along the berm downwind slope and along the ditch upwind cut because of wind flow separation [see p2, p3, and p4 in Fig. 10(b)]. The gradual accumulation of sand within the SMM body progressively moves the separation and reattachment points downwind and upwind, respectively. This results in the shrinking of the clockwise vortex up to its vanishing. The adjustment of the wind flow features around the SMM modifies in turn $\partial u/\partial z|_{z=0}$ and, therefore, erosion and deposition zones along the SMM profile. Accordingly, sand is transported up to the ditch downwind slope, slightly depositing on it, and eventually escaping from the SMM.

To assess the reaching of equilibrium conditions, the convergence of incoming Q_0 and outgoing Q_1 is visually checked for growing dimensionless time units $t^* = tu_{h_b}/h_b$. The dimensionless ratio Q_1/Q_0 sampled at every second is plotted in Fig. 10(d) for each performed ETD simulation. In particular, Q_0 is evaluated in open field, and Q_1 is evaluated just downwind the ditch. Overall, Q_1/Q_0 monotonically increases before reaching a plateau. The dimensionless time at which convergence is reached decreases with increasing filling level. This is primarily due to sedimented sand closer to the position at which Q_1 is evaluated for high filling levels. Once quasisteady sand transport is reached, LCP can be evaluated. The resulting life-cycle performance e_1 is plotted in Fig. 10(e) for increasing filling ratios $V_1/V_{f,1}$. The trend of e_1 reflects the wind flow pattern variation induced by sand morphodynamics. e_1 is initially constant and maximum for $V_1/V_{f,1} < 0.3$, i.e., the majority of sand is accumulated on the upwind side of the berm. After that, e_1 starts decreasing when sand consistently reaches the berm downwind slope and the vortex size decreases.

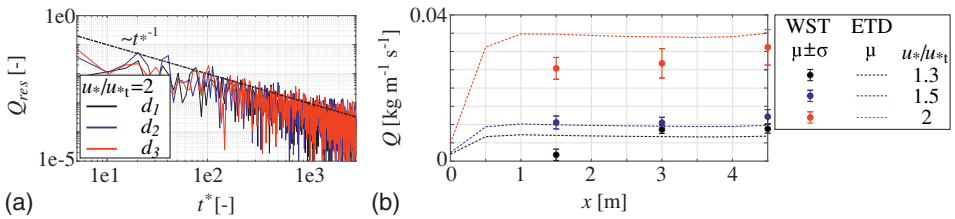

Fig. 9. Sand transport rate: convergence of Q through: (a) the weighted residual Q_{res} for $u_*/u_{*t} = 2$; and (b) streamwise variation of Q from WST measurements and ETD simulations.

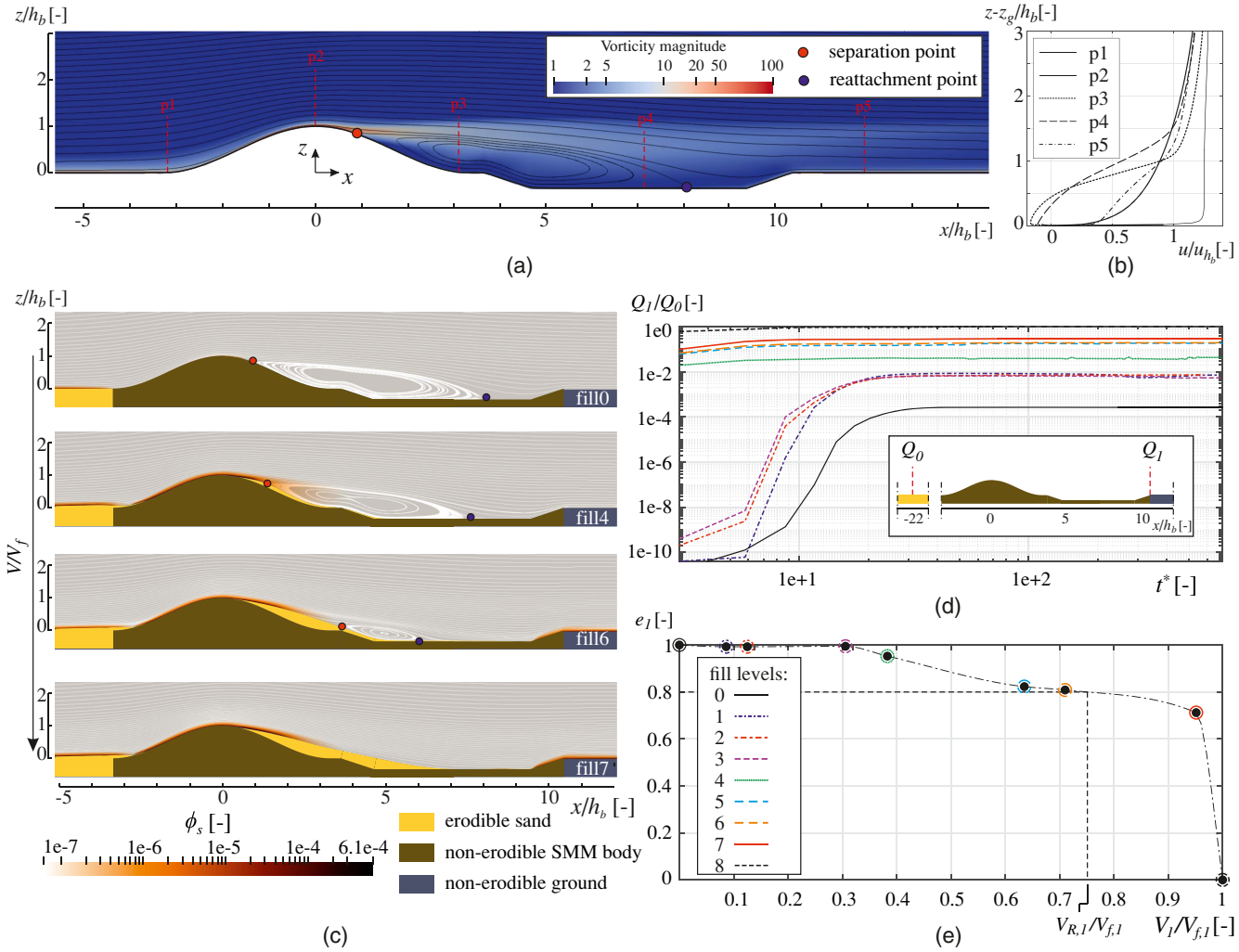

Fig. 10. Wind-sand flow features around the SMM: (a) streamlines and vorticity magnitude around the clean SMM; (b) vertical profiles of wind speed at different positions across the clean SMM; (c) sand concentration fields with wind flow streamlines for increasing filling levels; (d) convergence of incoming and outgoing transport rate; and (e) life-cycle performance of the SMM.

As soon as the recirculation region disappears and the sand reaches the ditch downwind slope, e_1 drops to zero. The SMM resistant sand volume $V_{R,1}$ is then identified as the accumulated volume for which the efficiency drops to 80% of the initial value, i.e., $V_{R,1} = 12.02\ \mathrm{m}^3/\mathrm{m}$.

Windblown Sand Action and SMM Life-Cycle Cost

Windblown sand transport attacks the railway line from the SE and NW sides. Figs. 11(a–d) provide the detailed description of incoming wind through the wind rose of U_{10}: (1) the wind speed time histories, (2) together with their probability density functions $f_{U_{10}}$, (3) direction frequencies f_θ, and (4) by referring to SE and NW sides. The Weibull-shaped $f_{U_{10}}$ are almost equivalent on both sides of the alignment, whereas wind occurrences are higher on the NW side. Because of that, the NW side is expected to be the most sensitive to windblown sand action. Fig. 11(e) shows the probability density function of the threshold shear velocity for sand transport $f_{u_{*t}}$.

The time growing windblown sand action on each infrastructure component is assessed by means of Monte Carlo simulations based on the bootstrapping technique, accounting for about $65 \times 10^{+6}$ numerical realizations. The resulting probabilistic windblown sand action on the NW side of the track is plotted in Figs. 11(f–h) through the mean value μ_{V_i}, the 5th percentile $p5_{V_i}$, and 95th percentile moved, and some probability density functions f_{V_i}. The time-constant $V_{R,i}$ is plotted as well to extrapolate the time increasing failure probability. For each component, the trend of V_i is nonlinear monotonic increasing and tends to the horizontal asymptote defined by the obstacle nominal capacity $V_{f,i}$. Once V_i realizations reach $V_{R,i}$, the probability of failure monotonically increases [Figs. 11(i–k)]. The characteristic times of failure $T_{k,i}$ of SMMs, embankment, and track correspond to the time at which the kth percentile pk_{V_i} curve crosses $V_{R,i}$. In Figs. 11(i–k), $T_{95,i}$ and $T_{5,i}$ are shown. For any considered $p_{f,k}$, failure occurs in chronological order on the SMM, then on the embankment, and finally on the track. In particular, on the NW side of the track, sand maintenance shall be planned every 7–8 months on the SMM, every 11–13 months on the embankment, and every 2.2–2.4 years on the track. It is worth stressing that exceptional sandstorm events are not taken into account by the present modeling framework.

To assess the economic impact of the SMM implementation along the railway service life, the LCCA is carried out. The unmitigated design scenario is retained for reference to assess the extra costs and savings.

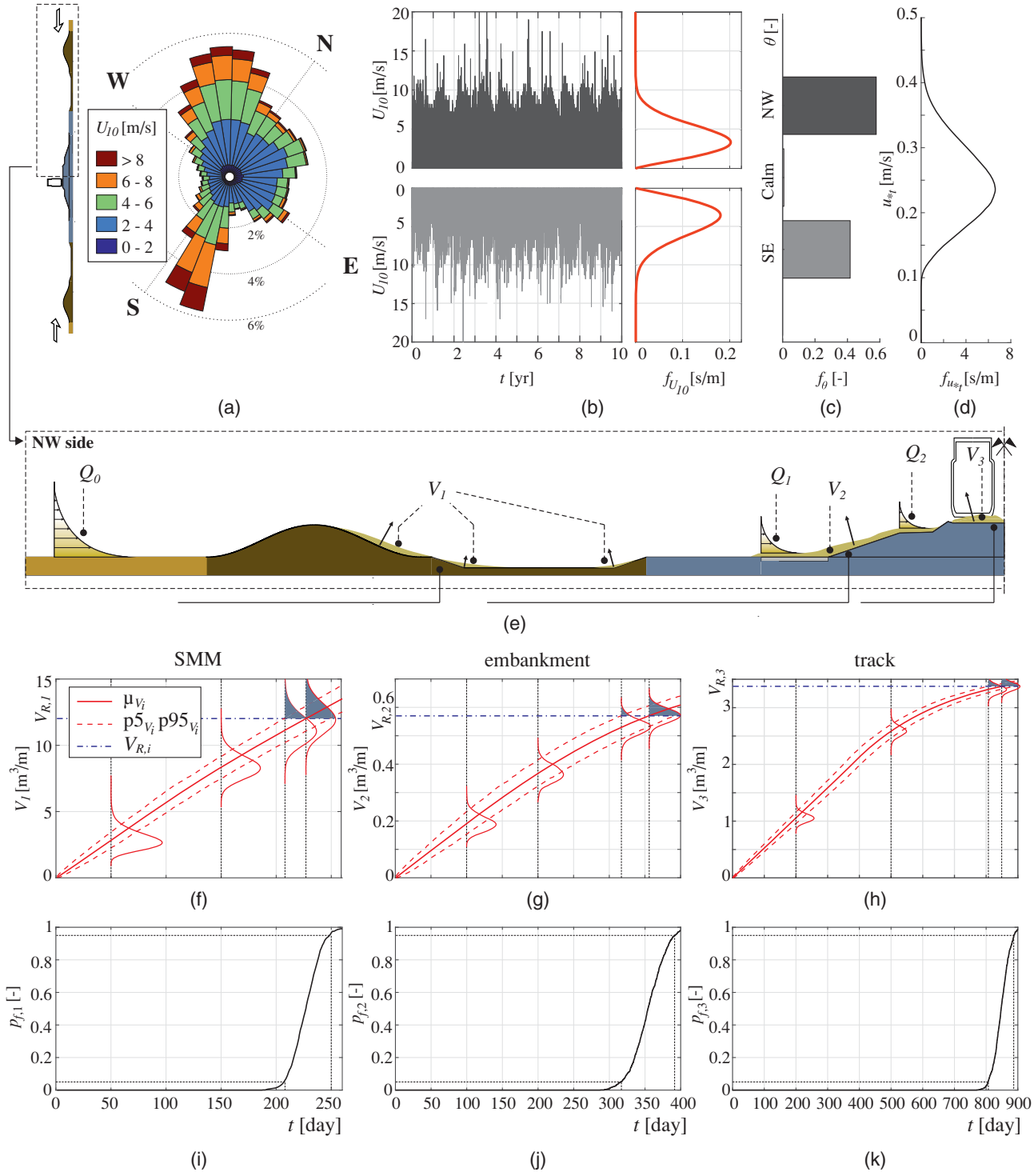

Fig. 11. Windblown sand action on SMM: (a–d) embankment and track on NW side of the alignment; (e) incoming wind statistics, threshold shear velocity probability density function; (f–h) time-growing probabilistic accumulated volumes; and (i–k) and related probabilities of failure.

Fig. 12 plots the cumulated extra costs and savings per kilometer of alignment $\Delta c(t) = c_0(t) - c(t)$ together with the normalized costs $c(t)/c_0(t)$ considering both sides of the railway line, being $c_0(t)$ the cumulated sand maintenance costs resulting from the unmitigated scenario. Environmental uncertainties, embodied by u_*, θ, and u_{*t} variability, are transposed into the LCCA by adopting $T_{k,i}$ resulting from different windblown sand action statistics, i.e., $p5_{V_i}$, $p95_{V_i}$, and μ_{V_i}. This in turn leads to the probabilistic description of Δc and c/c_0. The design and construction of the SMM involve initial additional costs. However, they are low if compared with sand maintenance costs and the break-even time (i.e., time at which $c = c_0$) takes place after about 3–5 years from completion. Depending on the chosen performance level, costs variation is significant. The savings with respect to the unmitigated scenario after 20 years amount to about \$2–\$4 million/km, i.e., from 40% to 50% the cost of the unmitigated railway. Finally, they increment up to about \$5.6–\$9.5 million/km after 100 years, i.e., 50%–60% of the cost of the unmitigated scenario. The average cost of civil

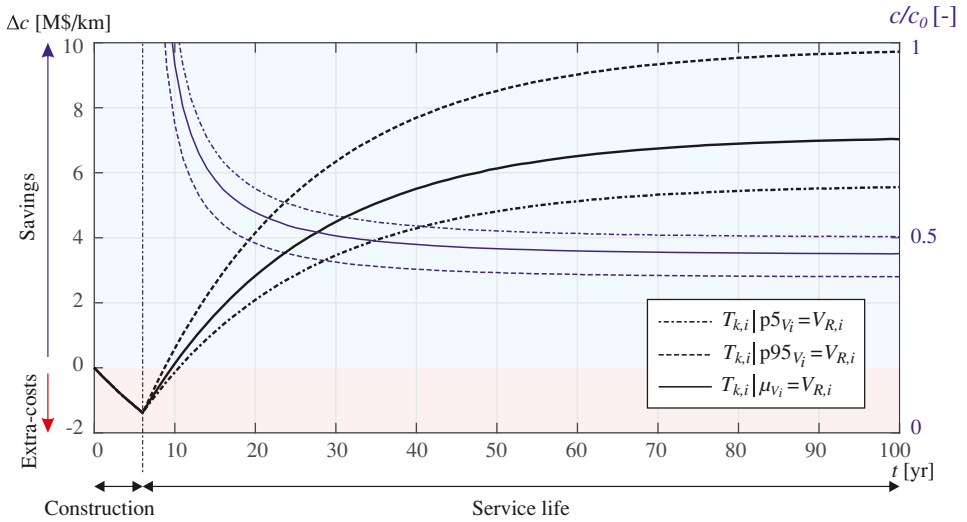

Fig. 12. Life-cycle cost analysis: railway mitigated by berm and ditch SMM versus unmitigated design scenario.

works, track works, and construction contract for Ethiad railway stage two package D amounts to about $8.6 million/km (Railway Technology 2019). As a result, sand maintenance costs and savings are relevant even if compared with both the railway infrastructure worth and the SMM design and construction costs.

In a (SULS) performance level perspective, high percentiles of windblown sand action shall be considered. However, the gap between LCCA curves reflects the uncertainty in windblown sand action and depicts the windblown sand induced costs and SMM induced savings in a conservative perspective. Furthermore, it demonstrates that a careful description of randomness in windblown sand action is fundamental to infer windblown sand induced costs.

Conclusion

The present study introduces a novel hybrid approach to assess the life-cycle performance and cost analysis of SMMs for the design of infrastructures in sandy regions and the retrofitting of existing ones. Within an engineering design perspective, the technical applicability of this novel approach has been demonstrated by referring to a case study dealing with a desert railway protected by a design solution against windblown sand action.

Open field windblown sand transport is characterized through wind-sand tunnel tests on a flat sand bed. Multiphase wind-sand computational simulations are tuned on WST measurements and put into practice to assess the full-scale SMM life-cycle performance for the first time. Windblown sand action is then quantified by considering uncertainties related to wind and sand subfields in the specific building site. A time-variant reliability analysis is performed to assess characteristic times of failure and plan life-cycle sand removal maintenance on any infrastructure component, i.e., the SMM, the embankment, or the track. Finally, a life-cycle cost analysis is adopted as a design tool to quantify the economic impact of the SMM design.

From the obtained results, some general comments can be drawn in an SMM hybrid performance assessment and design perspective. First, the characterization of windblown sand transport and quantification windblown sand action is of paramount importance for civil structures and infrastructures in sandy environments, such as SMMs. In this context, the combination of WST tests and ETD simulation allow to: (1) overcome WST shortcomings resulting from the testing of scale SMMs (Raffaele et al. 2021), and (2) assess SMM life-cycle performance in virtual full-scale conditions. In turn, this would allow toially replace and/or assist expensive field tests, usually incompatible with infrastructure designer/stakeholders time requirements. Second, the robust design and assessment of SMMs involve the accurate estimation of windblown sand action and SMM life-cycle cost. This implies in turn the correct estimation of the SMM life-cycle performance and wind-sand field variability. This is in analogy with the well-known wind engineering analysis chain first introduced by Davenport (1961), in which each chain link is crucial for the correct assessment of action and effects on structures.

Given the wide research field, several experimental-computational research perspectives arise. In particular: (1) the ETD model can be improved by including momentum balance of the sand phase and turbulence corrections. This would allow to model the two-way interaction between sand and wind phases so to correctly simulate wind and sand velocity close to the ground. However, two-way coupling models are difficult to be set up due to the number of modeling parameters and high computational cost. As a result, they are not commonly used for engineering problems (Lo Giudice et al. 2019); (2) despite the overall good SMM life-cycle performance, the railway land width should always be minimized to minimize in turn the soil consumption and the related expected costs of land expropriation. The adoption of the investigated SMM implies a large railway land footprint, equal to about 130 m. As such, berm and ditch geometry variations but also other SMM solutions meeting such a requirement are worth to be investigated; (3) in a fully probabilistic approach perspective, it is worth considering the randomness of uncertain LCCA setup parameters, such as discount rate and unit costs, to investigate the uncertainty propagation to the life cycle cost; (4) from Bruno et al. (2018a) and Horvat et al. (2021), we can conjecture that clean SMMs performs better at high wind speed and under orthogonal winds. As such, further 3D ETD simulations are envisaged to evaluate the SMM life-cycle performance under yawed winds and for different wind speeds. The thorough description of LCP according to wind directionality and magnitude will allow in turn to refine the estimation of the life-cycle cost; (5) in an even more general perspective, this study paves the way towards a full hybrid approach to SMM performance assessment. In this framework, ETD simulations shall be always fully validated against scale WST tests. As a result, highly

reliable WST tests on surface-mounted SMMs are required to characterize the wind flow, sand transport, and sand morphodynamics around them. In a fully hybrid performance assessment perspective, this will allow in turn to quantify the experimental distortion of life-cycle performance by recurring to full-scale constraints-free ETD simulations (Raffaele et al. 2021).

Data Availability Statement

Some or all data, models, or code generated or used during the study are proprietary or confidential in nature and may only be provided with restrictions. Available items: experimental wind-sand tunnel data. Restricted items: erosion-transport-deposition model code is restricted by a nondisclosure agreement.

Acknowledgments

The study has been developed in the framework of the MSCA-IF-2019 research project Hybrid Performance Assessment of Sand Mitigation Measures (HyPer SMM, hypersmm.vki.ac.be). This project has received funding from the European Union's Horizon 2020 research and innovation program under the Marie Sklodowska-Curie grant Agreement No. 885985. In particular, we acknowledge J. van Beeck, S. Buckingham from the von Karman Institute for Fluid Dynamics, and S. Khris, A. Lo Giudice, R. Nuca from Optiflow Company and Politecnico di Torino for the helpful discussions about the topics of the study. The study has been jointly developed in the framework of the Windblown Sand Modeling and Mitigation (WSMM, www.polito.it/wsmm) research, development, and consulting group established between Politecnico di Torino and Optiflow Company. Computational resources were provided by Optiflow Company.

References

Alghamdi, A. A., and N. S. Al-Kahtani. 2005. "Sand control measures and sand drift fences." *J. Perform. Constr. Facil.* 19 (4): 295–299. https://doi.org/10.1061/(ASCE)0887-3828(2005)19:4(295).

Anno, Y. 1984. "Requirements for modeling of a snowdrift." *Cold Reg. Sci. Technol.* 8 (3): 241–252. https://doi.org/10.1016/0165-232X(84)90055-7.

Basnet, K., G. Constantinescu, M. Muste, and H. Ho. 2014. "Method to assess efficiency and improve design of snow fences." *J. Eng. Mech.* 141 (3): 04014136. https://doi.org/10.1061/(ASCE)EM.1943-7889.0000871.

Blocken, B., T. Stathopoulos, and J. Carmeliet. 2007. "CFD simulation of the atmospheric boundary layer: Wall function problems." *Atmos. Environ.* 41 (2): 238–252. https://doi.org/10.1016/j.atmosenv.2006.08.019.

Bruno, L., and D. Fransos. 2015. "Sand transverse dune aerodynamic: 3D coherent flow structures from a computational study." *J. Wind Eng. Ind. Aerodyn.* 147 (Dec): 291–301. https://doi.org/10.1016/j.jweia.2015.07.014.

Bruno, L., D. Fransos, and A. Lo Giudice. 2018a. "Solid barriers for windblown sand mitigation: Aerodynamic behavior and conceptual design guidelines." *J. Wind Eng. Ind. Aerodyn.* 173 (Feb): 79–90. https://doi.org/10.1016/j.jweia.2017.12.005.

Bruno, L., M. Horvat, and L. Raffaele. 2018b. "Windblown sand along railway infrastructures: A review of challenges and mitigation measures." *J. Wind Eng. Ind. Aerodyn.* 177 (Jun): 340–365. https://doi.org/10.1016/j.jweia.2018.04.021.

Cebeci, T., and P. Bradshaw. 1977. *Momentum transfer in boundary layers*. Washington, DC: Hemisphere.

CEN (European Committee for Standardization). 2005. *Eurocode 1: Actions on structures—Part 1-4: General actions—Wind actions*. EN 1991-1-4. Brussels, Belgium: CEN.

Centre National d'Etudes et de Recherches Integrees du Batiment. 2013. *Document Technique Réglementaire C 2-4.7: Règlement Neige & Vent*. DTR C 2-4.7. Algiers, Algeria: Centre National d'Etudes et de Recherches Integrees du Batiment.

Davenport, A. G. 1961. "The application of statistical concepts to the wind loading of structures." *Proc. Inst. Civ. Eng.* 19: 449–471.

Dong, Z., H. Wang, X. Liu, and X. Wang. 2004. "The blown sand flux over a sandy surface: A wind tunnel investigation on the fetch effect." *Geomorphology* 57 (1–2): 117–127. https://doi.org/10.1016/S0169-555X(03)00087-4.

Edgell, H. S. 2006. *Arabian desert*. Berlin: Springer.

Fabrycky, W., and B. Blanchard. 1991. *Life cycle cost and economic analysis*. Englewood Cliffs, NJ: Prentice Hall.

Ferreira, A. D., A. M. G. Lopes, D. X. Viegas, and A. C. M. Sousa. 1995. "Experimental and numerical simulation of flow around two-dimensional hills." *J. Wind Eng. Ind. Aerodyn.* 54–55 (Feb): 173–181. https://doi.org/10.1016/0167-6105(94)00040-K.

Guo, Z., N. Huang, Z. Dong, R. Van Pelt, and T. Zobeck. 2014. "Wind erosion induced soil degradation in northern China: Status, measures and perspective." *Sustainability* 6 (12): 8951–8966. https://doi.org/10.3390/su6128951.

Harris, A. D., W. J. Grogg, A. Akoma, B. J. Hayes, R. F. Reidy, E. F. Imhoff, and P. C. Collins. 2015. "Revisiting (some of) the lasting impacts of the liberty ships via a metallurgical analysis of rivets from the SS 'John W. Brown'." *Jom* 67 (12): 2965–2975. https://doi.org/10.1007/s11837-015-1668-1.

Ho, T. D., A. Valance, P. Dupont, and A. O. El Moctar. 2011. "Scaling laws in aeolian sand transport." *Phys. Rev. Lett.* 106 (9): 094501. https://doi.org/10.1103/PhysRevLett.106.094501.

Horvat, M., L. Bruno, and S. Khris. 2021. "CWE study of wind flow around railways: Effects of embankment and track system on sand sedimentation." *J. Wind Eng. Ind. Aerodyn.* 208 (Jan): 104476. https://doi.org/10.1016/j.jweia.2020.104476.

Horvat, M., L. Bruno, S. Khris, and L. Raffaele. 2020. "Aerodynamic shape optimization of barriers for windblown sand mitigation using CFD analysis." *J. Wind Eng. Ind. Aerodyn.* 197 (Feb): 104058. https://doi.org/10.1016/j.jweia.2019.104058.

Hotta, S., and K. Horikawa. 1990. "Function of sand fence placed in front of embankment." In *Proc., 22nd Int. Conf. on Coastal Engineering*, 2754–2767. Reston, VA: ASCE.

Ierimonti, L., L. Venanzi, and L. Caracoglia. 2018. "Life-cycle damage-based cost analysis of tall buildings equipped with tuned mass dampers." *J. Wind Eng. Ind. Aerodyn.* 176 (May): 54–64. https://doi.org/10.1016/j.jweia.2018.03.009.

Iversen, J. D., and K. D. Rasmussen. 1994. "The effect of surface slope on saltation threshold." *Sedimentology* 41 (4): 721–728. https://doi.org/10.1111/j.1365-3091.1994.tb01419.x.

Kok, J. F., E. J. R. Parteli, T. I. Michaels, and D. B. Karam. 2012. "The physics of wind-blown sand and dust." *Rep. Prog. Phys.* 75 (10): 106901. https://doi.org/10.1088/0034-4885/75/10/106901.

Kubilay, A., D. Derome, B. Blocken, and J. Carmeliet. 2013. "CFD simulation and validation of wind-driven rain on a building facade with an Eulerian multiphase model." *Build. Environ.* 61 (Mar): 69–81. https://doi.org/10.1016/j.buildenv.2012.12.005.

Launder, B. E., and D. B. Spalding. 1974. "The numerical computation of turbulent flows." *Comput. Methods Appl. Mech. Eng.* 3 (2): 269–289. https://doi.org/10.1016/0045-7825(74)90029-2.

Le, V., and L. Caracoglia. 2019. "Life-cycle cost analysis of a point-like structure subjected to tornadic wind loads." *J. Struct. Eng.* 146 (2): 04019194. https://doi.org/10.1061/(ASCE)ST.1943-541X.0002480.

Liu, B., J. Qu, W. Zhang, and G. Qian. 2011. "Numerical simulation of wind flow over transverse and pyramid dunes." *J. Wind Eng. Ind. Aerodyn.* 99 (8): 879. https://doi.org/10.1016/j.jweia.2011.06.007.

Lo Giudice, A., R. Nuca, L. Preziosi, and N. Coste. 2019. "Wind-blown particulate transport: A review of computational fluid dynamics models." *Math. Eng.* 1 (3): 508–547. https://doi.org/10.3934/mine.2019.3.508.

Lo Giudice, A., and L. Preziosi. 2020. "A fully Eulerian multiphase model of windblown sand coupled with morphodynamic evolution: Erosion, transport, deposition, and avalanching." *Appl. Math. Model.* 79 (Mar): 68–84. https://doi.org/10.1016/j.apm.2019.07.060.

Menter, F. R., M. Kuntz, and R. Langtry. 2003. "Ten years of industrial experience with the SST turbulence model." In Vol. 4 of *Proc., 4th Int. Symp. on Turbulence, Heat and Mass Transfer: Turbulence Heat and Mass Transfer Series*, edited by K. Hanjalić, Y. Nagano, and J. Tummers, 1208. Antalya, Turkey: Begell House.

Meroney, R. N. 2016. "Ten questions concerning hybrid computational/physical model simulation of wind flow in the built environment." *Build. Environ.* 96 (Feb): 12–21. https://doi.org/10.1016/j.buildenv.2015.11.005.

O'Rourke, M., A. DeGaetano, and J. D. Tokarczyk. 2005. "Analytical simulation of snow drift loading." *J. Struct. Eng.* 131 (4): 660–667. https://doi.org/10.1061/(ASCE)0733-9445(2005)131:4(660).

Phillips, D. A. 2011. "Analysis of potential sand dune impacts on railway tracks and methods of mitigation." Accessed July 10, 2021. http://www.iktissadevents.com/files/events/gtrc/1/presentations/d2-s8-duncan-phillips.pdf.

Plaza, J. S., M. Lombardero Barceló, and P. Rodríguez de Lema Tapetado. 2012. "Sand and wind: An outline of the study of aeolian action on infrastructure with reference to Haramain High Speed Railway, Makkah–Al-Madinah." *Revista de Obras Públicas* 159 (3537): 7–36.

Preziosi, L., D. Fransos, and L. Bruno. 2015. "A multiphase first order model for non-equilibrium sand erosion, transport and sedimentation." *Appl. Math. Lett.* 45 (Jul): 69–75. https://doi.org/10.1016/j.aml.2015.01.011.

Raffaele, L., and L. Bruno. 2019. "Windblown sand action on civil structures: Definition and probabilistic modelling." *Eng. Struct.* 178 (Jan): 88–101. https://doi.org/10.1016/j.engstruct.2018.10.017.

Raffaele, L., and L. Bruno. 2020. "Windblown sand mitigation along railway megaprojects: A comparative study." *Struct. Eng. Int.* 30 (3): 355–364. https://doi.org/10.1080/10168664.2020.1714530.

Raffaele, L., L. Bruno, F. Pellerey, and L. Preziosi. 2016. "Windblown sand saltation: A statistical approach to fluid threshold shear velocity." *Aeolian Res.* 23 (Dec): 79–91. https://doi.org/10.1016/j.aeolia.2016.10.002.

Raffaele, L., L. Bruno, and D. J. Sherman. 2020. "Statistical characterization of sedimentation velocity of natural particles." *Aeolian Res.* 44 (Jun): 100593. https://doi.org/10.1016/j.aeolia.2020.100593.

Raffaele, L., J. van Beeck, and L. Bruno. 2021. "Wind-sand tunnel testing of surface-mounted obstacles: Similarity requirements and a case study on a sand mitigation measure." *J. Wind Eng. Ind. Aerodyn.* 214 (Jul): 104653. https://doi.org/10.1016/j.jweia.2021.104653.

Railway Technology. 2019. "Etihad Rail awards $1.25B contract for Package D work." Accessed July 10, 2021. https://www.railway-technology.com/news/etihad-rail-contract-package-d/.

Ribeiro, A. S., A. L. L. Silva, and A. M. P. de Jesus. 2011. "Evolution of fatigue history." In *Proc., Congresso Brasileiro de Engenharia Mecânica*. Hampton, IA: ABCM.

Richards, P., and S. Norris. 2011. "Appropriate boundary conditions for computational wind engineering models revisited." *J. Wind Eng. Ind. Aerodyn.* 99 (4): 257–266. https://doi.org/10.1016/j.jweia.2010.12.008.

Sañudo-Fontaneda, L. A., D. Castro-Fresno, J. J. Coz-Díaz, and J. Rodriquex-Hernandez. 2011. "Classification and comparison of snow fences for the protection of transport infrastructures." *J. Cold Reg. Eng.* 25 (4): 162–181. https://doi.org/10.1061/(ASCE)CR.1943-5495.0000031.

Tominaga, Y. 2018. "Computational fluid dynamics simulation of snowdrift around buildings: Past achievements and future perspectives." *Cold Reg. Sci. Technol.* 150 (Jun): 2–14. https://doi.org/10.1016/j.coldregions.2017.05.004.

Tominaga, Y., T. Okaze, and A. Mochida. 2018. "Wind tunnel experiment and CFD analysis of sand erosion/deposition due to wind around an obstacle." *J. Wind Eng. Ind. Aerodyn.* 182 (Nov): 262–271. https://doi.org/10.1016/j.jweia.2018.09.008.

Valance, A., K. R. Rasmussen, A. O. El Moctar, and P. Dupont. 2015. "The physics of aeolian sand transport." *C.R. Phys.* 16 (1): 105–117. https://doi.org/10.1016/j.crhy.2015.01.006.

White, B. R. 1996. "Laboratory simulation of aeolian sand transport and physical modeling of flow around dunes." *Ann. Arid Zone* 35 (3): 187–213.

Xin, G., N. Huang, J. Zhang, and H. Dun. 2021. "Investigations into the design of sand control fence for Gobi buildings." *Aeolian Res.* 49 (Feb): 100662. https://doi.org/10.1016/j.aeolia.2020.100662.